MOTION TRACKING OF THE OUTER TIPS OF MICROTUBULES

Stathis Hadjidemetriou[a], *Derek Toomre*[b], *James Duncan*[c]

[a]*NCIRE/VA UCSF, San Francisco, CA 94121,*
[b]*Yale University, Department of Cell Biology, New Haven, CT 06520,*
[c]*Yale University, Department of Biomedical Engineering and Diagnostic Radiology, New Haven, CT 06520*

ABSTRACT

Microtubules are tubular biopolymers of the cytoplasm. They play numerous critical roles in a cell such as providing mechanical support and structural tracks for the anchoring and transport of chromosomes, organelles, and vesicles. They also form the microtubule assembly, which is critical for the coordination of cell division and migration. Abnormal function of the assembly is involved in cell pathology such as neurodegenerative diseases and cancer. To date the study of the dynamics of the microtubule assembly has been mostly qualitative by visual inspection. Some quantitative statistics have been computed for the most dynamic part of the assembly, namely, the microtubule outer tips located close to the cell cortex. Typically, the locations of those tips are manually annotated in a time sequence, which is very tedious. In this work we have developed a method to automatically track microtubule tips so as to enable a more extensive and higher throughput quantitative study of the microtubule assembly. Our approach first uses the entire frame sequence to estimate the region where a tip is expected to lie. In that region a tip feature is computed for all time and used to form the tip trajectory. Last, we evaluate our method with phantom as well as real data. The real data show fluorescently tagged living cells imaged with epifluorescent microscopy or confocal microscopy.

Keywords: Confocal microscopy, microtubule plus tips, microtubule dynamics, tubular structure segmentation, motion tracking.

1. INTRODUCTION

1.1. Significance of Microtubules

Microtubules are biopolymers of the cytoplasm. They have a diameter of $\approx 25\ nm$ and are composed of $10 - 15$ tubulin protofilaments [1]. In mammalian interphase cells one end is anchored at an organelle called the microtubule organizing center (MTOC), which is positioned in the cell center next to the nucleus. Hundreds of microtubules emerge radially from the MTOC like spokes out of a wheel. Two illustrations of their assembly are shown in figure 1. In addition to providing structural stability the microtubules also serve as delivery tracks for the active transport of organelles and vesicles. For instance, in a neuron they move vesicles out to the terminals of centimeter long axons in minutes to hours, whereas free diffusion would take years. They also act as potential mediators of cell protein signalling. The microtubules can come in close proximity to the cell cortex and dynamically probe the cell periphery by rapidly growing with polymerization and shrinking with depolymerization [1, 2, 3]. Their outer tips are pivotal in chromosome repositioning during mitosis as well as cell migration [4].

Microtubules also play critical roles for cells in pathological states. Cell migration is essential for wound healing. Abnormalities in the microtubule assembly have been correlated with the severity of Alzheimer's symptoms [5]. Cancerous cells exhibit abnormalities in microtubule function related to cell division. Thus, microtubules have been identified as an important target for anticancer drugs [6]. Chemical entities such as the taxanes inhibit

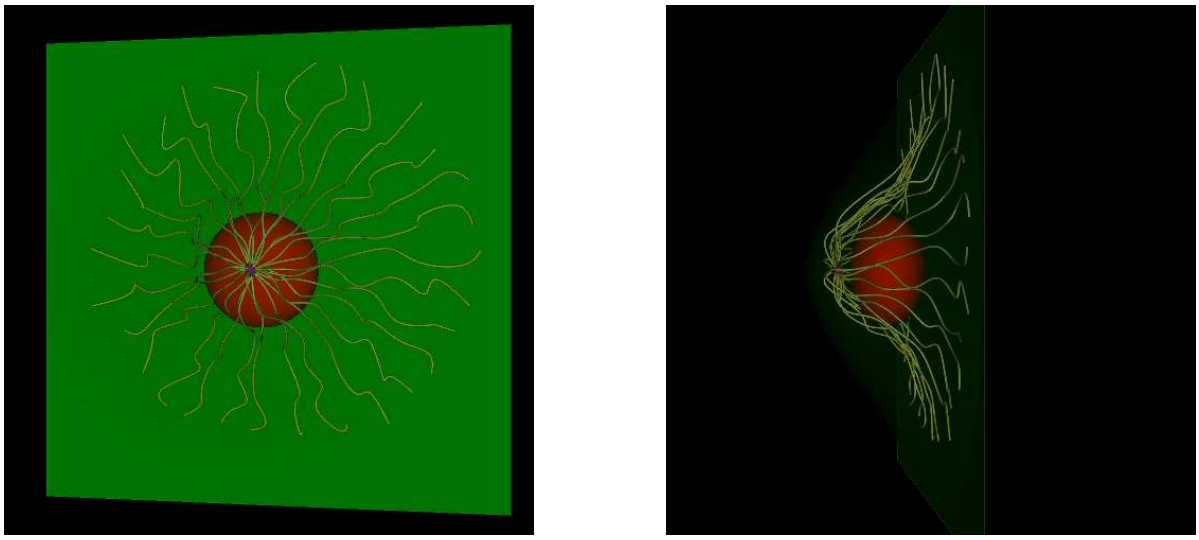

Fig. 1. Two viewpoints of a simulation of the microtubule assembly. The microtubules in yellow originate from the microtubule organizing center near the center of the cell, next to the nucleus. They end close to the cell membrane.

the polymerization of microtubules. Thus, they stabilize the assembly and retard cancer growth. Microtubule drugs are used in the treatment of a variety of tumor types such as leukemia, cancers of the lymphatic system, and breast cancer. Several novel anticancer compounds with a similar effect on the microtubules are in active clinical development with the goal of identifying new drugs with improved specificity. It is essential to elucidate their specific effects on the microtubule assembly. The latter with the goal of improving the therapeutic index with reduced toxicity [6]. Current in vivo screening is tedious as microtubule data is analyzed by hand. Automation can facilitate both basic science analysis of microtubules as well as enable higher throughput screening of new microtubule drugs. Thus, the general goal of the automated processing of data of the microtubule assembly is to efficiently quantify its structure and dynamic behavior.

1.2. Related Work on Segmentation and Motion Tracking of Microtubules and Tubular Structures

To our knowledge the study of the microtubule assembly in microscopy and in particular in epifluorescent and confocal microscopy data has only been done qualitatively by observation [7, 8]. Some limited quantitative statistics of the microtubules have typically been reported from manual annotation [9, 10, 11, 2, 3]. The manual approach is time consuming and limiting. Only a small number of clearly distinguished microtubules are tracked for a limited temporal extent. Human operators annotate the position of the tip. That data is later used to compute the rates of polymerization and depolymerization by assuming that the microtubules are straight lines between the tip point and an arbitrary reference point in the image. Moreover, manual tracking is subjective and is not reproducible. The automatic processing of data showing the motion of the microtubule assembly has also been limited in the number of tips tracked, the temporal extent of the tracking, and the number of sequences on which tracking has been evaluated [12, 13, 14, 15, 16, 17].

Algorithms for the processing of the motion of tubular structures typically consist of preprocessing, tubular segmentation, motion tracking, and summarization of the motion. Some preprocessing techniques have been edge filtering [18], corner filtering, line filtering [19], histogram based intensity thresholding [20], as well as morphological operations [21]. A combination of such techniques has been used extensively for the extraction of microtubules and other subcellular filamentous structures. A typical sequence of steps has been to enhance the

images with filtering, threshold the images based on intensity, and subsequently detect the tubular structure and their tips with morphological operations [12, 15, 16, 17, 22]. A major limitation of these approaches has been the requirement to have an intensity threshold to segment the foreground of the microtubule assembly from the background. The selection of the threshold is difficult to do systematically. The threshold selection in a time sequence is also complicated by the depletion of the fluorescence with time. Moreover, morphological operations can introduce an error in the estimate of the tip location.

Several alternative approaches to the segmentation of a tubular structure have been suggested that do not require an intensity threshold. Such an approach has been to start from a single point and perform sequential intensity tracking [13, 23, 24], or sequential vector field tracking [25]. These segmentation algorithms are based on local computations and can be noise sensitive. An alternative approach to segmentation of tubular structures has been the use of minimal global paths [26, 27, 28, 29, 30, 31, 32, 33]. These paths are streamlines of cost maps computed by accumulating intensity or vector field information. The global approaches to segmentation of a tubular structure that are based on monotonically growing potentials require the specification of both end points of the structure [27, 29, 30, 32]. The minimal global direct paths do not require a threshold and are more robust to noise. However, they are unable to represent the local characteristics of filamentous structures or resolve clutter of filamentous structures in their subcellular assemblies. In this work we combine the local sequential and the minimal path approaches. We use a minimal path approach to take advantage of its noise robustness and its ability to favor the differential geometric properties of the microtubule axis. However, we apply the minimal path approach locally over spatially restricted regions. This improves its ability to represent local structure of microtubules.

The detection of the microtubule tip location is a difficult problem due to the low signal to noise ratio at that point. This is mainly a result of the diffraction during the imaging process, and the breakup of a microtubule at its outer tip point into its constituent protofilaments. The tip detection is also complicated by the curvature of the microtubule. The microtubule tip point in our work is characterized locally using level sets of minimal paths defined similarly as for microtubule segmentation. They are used because of their robustness to noise and their ability to represent local microtubule curvature.

Tubular segmentation techniques have been used in microscopy to extract other cellular biopolymers such as actin [20] and chromosomes [23], as well as neurites at the cellular level [34]. Several tubular structures have also been extracted at the organ imaging level such as vasculature from magnetic resonance angiography data [33], paths along the colon for virtual colonoscopy [26, 27, 28], white matter fibers from diffusion tensor imaging data [29, 32], and the bronchial tree [35].

A traditional approach to motion quantitation of microtubules, namely kymography [14], assumes that a microtubule moves predominantly along its axis. The cross section at a point along its axis is used to characterize the intensity variation as a wave. More recently, Saban et al suggested an automated tip tracking algorithm [16]. Their tracking algorithm, however, favors points along the microtubule axis rather than the tip points. Moreover, it requires an intensity threshold that is not set systematically [16]. There has also been work on motion tracking of tubular structures at the organ imaging level. Some examples have been the tracking of the motion of vasculature in coronary cineangiography [36], the retina in retinal imaging [37], and catheter monitoring [38].

In the literature the microtubule tip motion has been quantified by its speed, motion duration, and transition rates between polymerization and depolymerization [9, 10]. In this work we also suggest the use of the power spectral density of the microtubule length as a function of time. It can represent the cyclical changes between polymerization and depolymerization of a microtubule in steady state as well as the acceleration in the polymerization of a microtubule. Accurate automatic or semi-automatic quantification of microtubule dynamics allows a more extensive quantification of the dynamics in the time and the number of tips tracked. It also improves the accuracy of the estimates of the tip dynamics and makes the computations objective and reproducible. Moreover, it enables the measurement of the length of a microtubule along its axis. A reliable quantitative approach for automatic determination of the motion of microtubules and their outer tips has not been evident in the literature. In this work

we present an algorithm that addresses the problem of motion tracking of the microtubule outer tips and compute measures to meaningfully summarize their motion [9, 10].

1.3. Related Work in Microscopy

There has been extensive work on motion tracking in microscopy for particles that have the shape of dots such as individual atoms, cytoplasmic vesicles, and cytoplasmic organelles [39]. Typically dot tracking algorithms consist of a feature detection step and a trajectory linking step. The feature detection is usually performed with model based template filters such as wavelets [40]. Some of the trajectory linking techniques have been cross-correlation [41], distance between centers of mass [42], and distance between Gaussian functions fitted to intensity profiles [43]. Some of the main problems in the tracking of dots in microscopy have been the possible temporary disappearance of a dot from an image sequence, the possible spurious detection of dots in individual frames of a sequence, as well as the overlap of dots in some frames. These complications have been addressed at the trajectory linking step using advanced probabilistic techniques such as Kalman filtering [44, 45] and graph based approaches [46] between consecutive frames.

Another suggestion for trajectory linking has been to use spatiotemporal level sets [40]. This approach, however, can potentially lead to a trajectory progressing backward in time. Moreover, spatiotemporal tracking restricts the motion between two consecutive frames to be at most one voxel, which is the radius of the neighborhood used for the level set propagation. In general, spatiotemporal approaches in microscopy are also hampered by the bleaching of the fluorescence with time and the temporal smoothing that may lead to tip points that do not lie on the microtubules in some frames. Motion tracking in microscopy has also been used to track entire cytoplasmic assemblies [47, 48] and even entire cells [49]. Many researchers claim superresolution in localization [42]. In microscopy the motion of dots has been characterized by measures such as diffusivity and directionality [50, 51].

2. METHODS

We first summarize some properties of the microscopy data relevant to this work. Subsequently, we describe the various stages of the motion tracking algorithm [52]. A block diagram summarizing the algorithm is in figure 6.

2.1. Image Data

In vivo epithelial cells provide the substrate for this work. The cells were transfected with tubulin tagged with a fluorescent protein. They were imaged with epifluorescent microscopy or confocal microscopy to give a video sequence. The data was acquired for a 2D plane over time. The point spread functions are assumed to be Gaussians. The spatial resolution is $\approx 130\ nm/pixel$. In confocal microscopy the depth resolution is $\approx 500\ nm$. The low interframe time required to closely capture the dynamics of the microtubules keeps the signal to noise ratio low. In 2D data the microtubules can be approximated as bright ridges with a Gaussian cross section. The extent of the Gaussian within one standard deviation of the peak gives the effective microtubule width w. A microscopy sequence of duration $t = 0, \ldots, \tau - 1$ consists of frames represented by the map $\mathcal{V}_t : D \rightarrow \Re$ from a 2D domain D of dimension $\mathbf{x} = (x, y)$ to intensity.

2.2. Feature Detection

The frames of the sequence are viewed as gray value functions. They are enhanced using a line contrast feature based on the extrema of the second spatial Gaussian derivative [30, 53]. This feature is computed at all pixels of the sequence $\mathcal{V}_t(\mathbf{x})$ to give $\mathcal{I}'_t(\mathbf{x})$, $\forall \mathbf{x}, t$. The extrema of the second Gaussian derivatives at pixel $\mathbf{x}$ are computed from the eigenvector decomposition of the spatial Hessian matrix at that point to give the eigenvalues $\lambda_1(\mathbf{x})$ and

$\lambda_2(\mathbf{x})$. The line contrast feature is computed from:

$$\mathcal{I}'_t(\mathbf{x}) = \begin{matrix} -\lambda_i(\mathbf{x}) \\ 0 \end{matrix} \quad \begin{matrix} if \quad \lambda_i(\mathbf{x}) > \lambda_j(\mathbf{x}) \cap \lambda_i(\mathbf{x}) < 0 \quad , where \quad (i,j) = (1,2),(2,1) \\ otherwise. \end{matrix} \tag{1}$$

The image derivatives are computed with Gaussian derivative filters of standard deviation $\sigma = w$, where w is the microtubule width.

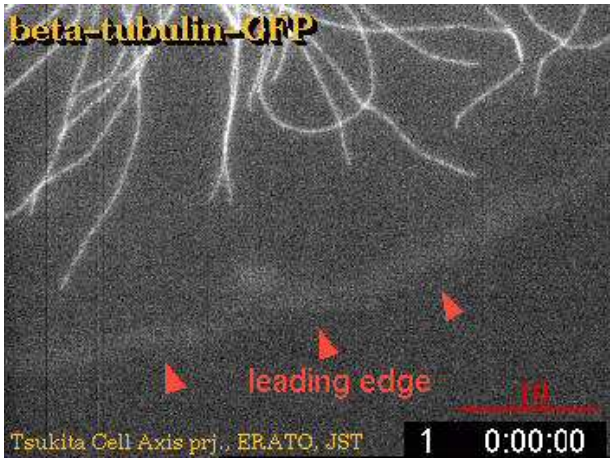

(a) First frame of a real sequence

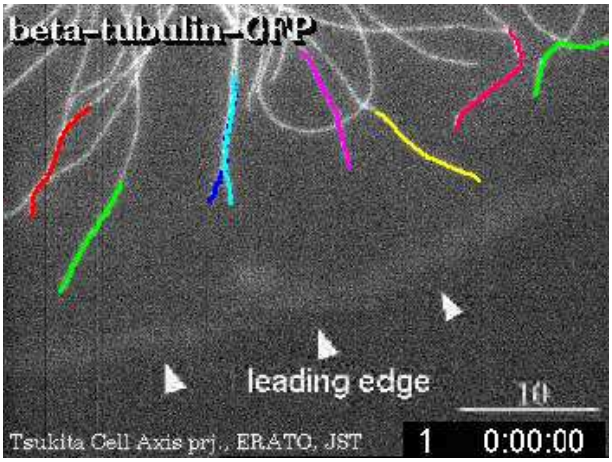

(b) Segmented microtubules over the first frame

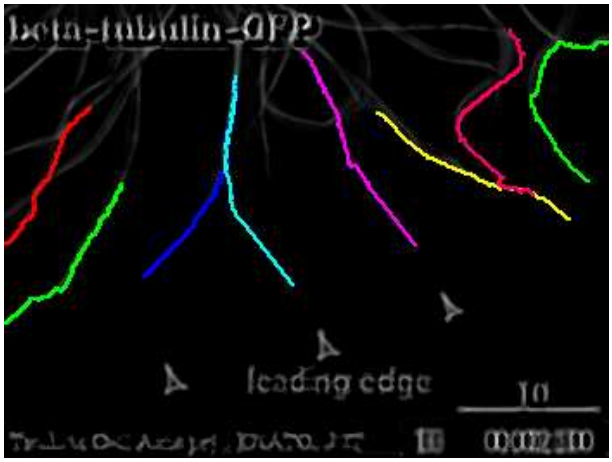

(c) Extrapolated microtubules over the average frame

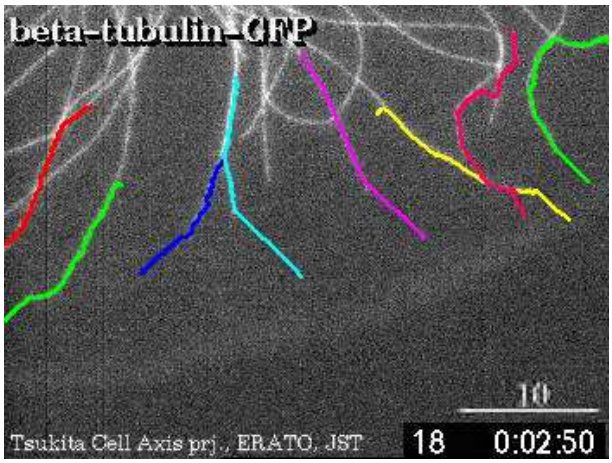

(d) Candidate tip points at the intermediate frame

Fig. 2. *The first frame of the sequence is in (a). The segmentations of the microtubules over this frame are shown in (b). The average frame together with the extrapolations of the microtubules computed based on it are shown in (c). These curves are subsequently refined for each frame. The curves expected to contain the tips at the intermediate,* 18^{th} *frame, of the sequence are shown in (d).*

2.3. Segmentation of a Microtubule

A microtubule is extracted in terms of consecutive segments [54]. Each segment is extracted based on its neighborhood $D_{segm} \in D$. The neighborhood is formed using a local coordinate system $(x^{segm}, y^{segm}) = (x, y) - O^{segm}$,

where O^{segm} is the origin. The origin for the extraction of the first segment is the tip point $\mathbf{x}_{tip,0}$ at the first frame of the sequence, $\mathcal{I}'_0$. The valid and non-null neighborhood is within the circle $\|(x^{segm}, y^{segm})\| \leq 4w$ and a surrounding annulus is nulled. The origin O^{segm} for the extraction of all subsequent segments is the most recently segmented point $\mathbf{x}_{rec}$. The valid neighborhood for the extraction of subsequent segments is also within the circle $\|(x^{segm}, y^{segm})\| \leq 4w$. Moreover, the x^{segm}-axis is the microtubule tangent and the neighborhood is limited to the region $x^{segm} \leq 2w$, where w is the microtubule width. Figure 3 shows a coordinate system centered at $\mathbf{x}_{rec}$.

A microtubule segment in domain D_{segm} of length l can be represented by the curve $\mathcal{S}(s) : [0, l] \rightarrow D_{segm}$, where s is the arc-length parameter. A microtubule segment has two boundary points $\mathcal{S}(0) = \mathbf{x}_0$ which is $\mathbf{x}_{rec}$ and $\mathcal{S}(l) = \mathbf{x}_1$ which satisfies $\mathbf{x}_1 \in \partial D_{segm}$. The set of all curves with these boundary points is $\mathcal{B}_{\mathbf{x}_0,\mathbf{x}_1}$. Every pixel at $\mathbf{x} = (x, y) \in D_{segm}$ is associated with cost Q. The pixel cost Q is the product of two factors. The first is proportional to the reverse intensity $Q_1 = 1 - \mathcal{I}'(\mathbf{x})/\mathcal{I}'_{max}$, where $\mathcal{I}'_{max} = \max_{\mathbf{x}} \mathcal{I}'(\mathbf{x})$. It is isotropic and favors microtubule fluorescence. The second factor, Q_2, is anisotropic and favors microtubule centerline. It uses directional parameters associated with every pixel, namely vectors $\mathbf{d}_1$ and $\mathbf{d}_2$, as well as scalars r_1 and r_2. The pixel cost is non-negative and is given by:

$$Q(\mathbf{x}, \mathbf{e}) = \left(1 - \frac{\mathcal{I}'(\mathbf{x})}{\mathcal{I}'_{max}}\right) \times \left(\frac{1}{\|\mathbf{e}\|} \sum_{i=1}^{i=2} \left\| \frac{\mathbf{d}_i.\mathbf{e}}{r_i + \epsilon} \right\| \right), \tag{2}$$

where ϵ is a very small regularizing constant, and $\mathbf{e}$ is a vector. The directional pixel parameters of Q are derived from the extrema of the second directional derivative. They are computed from the eigenvector decomposition of the Hessian matrix of second derivatives. The vectors $\mathbf{d}_1$ and $\mathbf{d}_2$ are set to the eigenvectors of the smaller eigenvalue and larger eigenvalue magnitudes, respectively. The scalars r_1 and r_2 are set to the magnitudes of the larger and smaller eigenvalues, respectively.

The set of curves $\mathcal{S} \in \mathcal{B}_{\mathbf{x}_0,\mathbf{x}_1}$ is associated with the cost functional:

$$E(\mathcal{S}) = \int_{\mathbf{x}_0}^{\mathbf{x}_1} Q(\mathcal{S}(s), \mathcal{S}'(s)) ds. \tag{3}$$

The curve of minimum E over the set $\mathcal{B}_{\mathbf{x}_0,\mathbf{x}_1}$ is the microtubule segment. It can be computed over the cumulative cost map of minimum possible values $U_0(\mathbf{x}) : D_{segm} \rightarrow \Re^+$ that starts at $\mathbf{x}_0$. That is, the minimal map is $U_0(\mathbf{x}) = \min_{\mathcal{S} \in \mathcal{B}_{\mathbf{x}_0,\mathbf{x}}} \{E(\mathcal{S}_{\mathbf{x}_0,\mathbf{x}})\}$. This relation can be combined with the differential of equation (3) to give the Hamilton-Jacobi equation:

$$\|\nabla U_0\| = Q. \tag{4}$$

This relation can be solved numerically to obtain the minimal cumulative cost U_0.

The numerical solution of equation (4) for $U_0(\mathbf{x})$ is computed in terms of consecutive level sets [27]. A level set $U_0(\mathbf{x}) = t$ is the closed curve $\mathcal{C}(v, t) : \Re^1 \rightarrow \Re^2$, where v is the arc-length parameter. The family $\mathcal{C}(v, t)$ over t is computed with the time evolution equation $\frac{\partial \mathcal{C}(v,t)}{\partial t} = \frac{\mathbf{d}(v,t)}{Q}$, where $\mathbf{d}(v, t)$ is the normal to $\mathcal{C}(v, t)$ [27]. It is initialized with a curve $\mathcal{C}(., 0) \equiv \partial D_{segm}$. The numerical solution visits each pixel once [55] and their costs $Q(\mathbf{x}, \mathbf{e})$ in equation (2) are minimized with respect to $\mathbf{e}$ originating from the eight-connected neighborhood. This minimization of Q is simple since it is a convex function of its parameters with a rhombus boundary [55, 56]. The retrieval of the pixels in a sequence is done efficiently with a priority heap [55]. A curve $\mathcal{S}'$ is extracted by starting from $\mathbf{x}_0 = \mathbf{x}_{rec}$ and proceeding along $\frac{\partial \mathcal{S}'}{\partial s} = -\nabla U_0$ to arrive at $\mathbf{x}_1 \in \partial D_{segm}$. The curve $\mathcal{S}'$ minimizes $E(\mathcal{S}_{\mathbf{x}_0,\mathbf{x}_1})$ and is appended to the microtubule $\mathcal{M}$. The microtubule extraction ends when it reaches length $l = 8w$.

2.4. Segmentation and Enhancement of the Microtubule Assembly

Several microtubule outer (+) tips $\mathbf{x}^i_{tip,0}$, $i = 0, \ldots, n-1$ can be selected at the first frame, $\mathcal{I}'_0$, of the sequence with a user-interface that involves a mouse. The algorithm described earlier for line extraction is used to extract the part

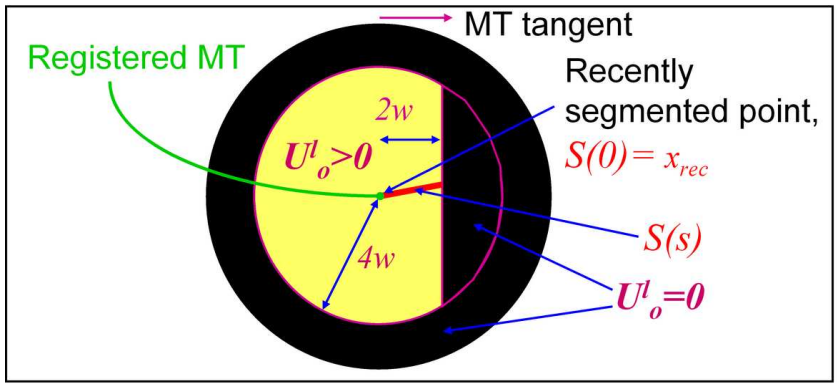

Fig. 3. A coordinate system centered at the most recently segmented point, $\mathbf{x}_{rec}$, of a microtubule. The valid region is in yellow surrounded by the null region in black.

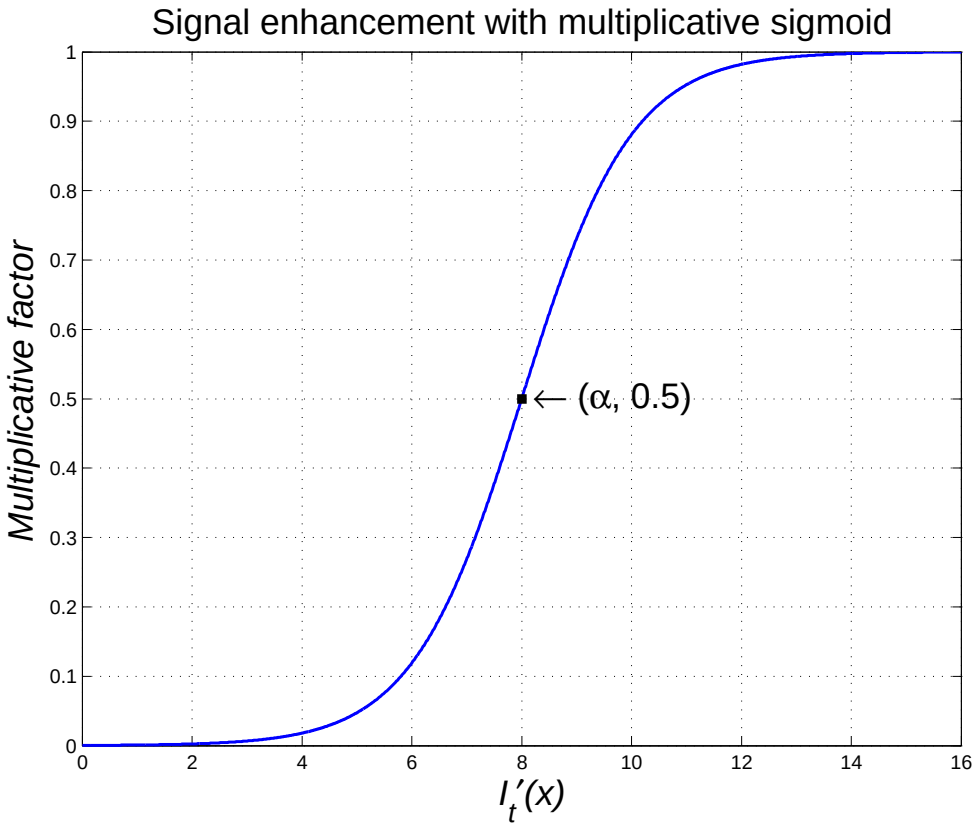

Fig. 4. The multiplicative sigmoid factor in equation (5), that is $\frac{1}{2}\left(\tanh\left(\frac{\mathcal{I}'_t(\mathbf{x})-\alpha}{2}\right)+1\right)$. It multiplies $\mathcal{I}'_t$ and transforms it to $\mathcal{I}_t$. The maximum multiplicative factor is one and hence it preserves the dynamic range of the image. The transformation enhances the signal to noise ratio. In this example $\alpha = 8$.

of the microtubules $\mathcal{M}^i$, $i = 0, \ldots, n-1$, close to the microtubule outer tip in the first frame. The union of all the microtubule segments $\mathcal{M}^i$, $\forall i$ gives the microtubule assembly $\mathcal{A}_0$ in the first frame of the sequence. The segmented microtubules of the image in figure 2 (a) are shown in figure 2 (b) in different colors. *The intensities over $\mathcal{A}_0$ give*

a distribution. A standard deviation below the mean of this distribution gives intensity $\alpha = \mu(\mathcal{A}_0) - \sigma(\mathcal{A}_0)$*, which is used to transform the intensities in the sequence with a multiplicative sigmoid function to give:*

$$\mathcal{I}_t(\mathbf{x}) = \mathcal{I}'_t \frac{1}{2}\left(\tanh\left(\frac{\mathcal{I}'_t(\mathbf{x}) - \alpha}{2}\right) + 1\right), \quad \forall \mathbf{x}, t. \tag{5}$$

This multiplicative sigmoid is shown in figure 4. Its maximum value is one and hence it preserves the dynamic range of the image. It also enhances the range of intensities that is larger than α *and attenuates the range of intensities that is lower than* α*. The range of intensities below* α *corresponds to the background. Thus, the intensity transformation further increases the signal to noise ratio in the sequence. Even though the background is attenuated it is not set to zero. The diffraction makes the cross section of a microtubule very similar to a Gaussian. The falloff of the intensities away from the microtubule axis is smooth and extends into the background. Thus, the background also contains information about the location of the microtubule axis. The transformation is monotonic and hence subsequent steps of the algorithm are more robust to the precise value of* α *compared to using the same intensity as a threshold to set the background to zero.* A block diagram of the algorithm is in figure 6. In that diagram the feature enhancement of the microtubules together with their segmentation are the first two steps.

2.5. Depolymerization and Polymerization Region of a Microtubule Outer Tip

The most active part of a microtubule is its outer tip. It probes the cytoplasm by polymerizing and depolymerizing [1]. The extent of the axial microtubule motion is much greater than the extent of the lateral one. This is particularly the case in depolymerization where the microtubule tip motion is a collapse along its axis. Thus, the trajectory of the outer tip in depolymerization lies along the microtubule axis in the frame where *the tracking* starts. This is the first frame of the sequence $\mathcal{I}_0$. *That is, the possible depolymerization trajectory of the* i^{th} *microtubule tip lies along its axis at* $t = 0$*,* $\mathcal{M}_0^i$. The farthermost point from $\mathbf{x}_{tip,0}^i$ along $\mathcal{M}_0^i$ is the innermost reference point, $\mathbf{x}_{inner}^i$, and is used for the computation of the microtubule outer tip depolymerization trajectory. This is shown in figure 5 (a). *To model the limited lateral motion that a microtubule can have we consider the region around* $\mathcal{M}_0^i$ *within* $\nu = 2w$ *to get region* D_d^i. That region is expected to contain the possible depolymerization trajectory of the i^{th} microtubule outer tip.

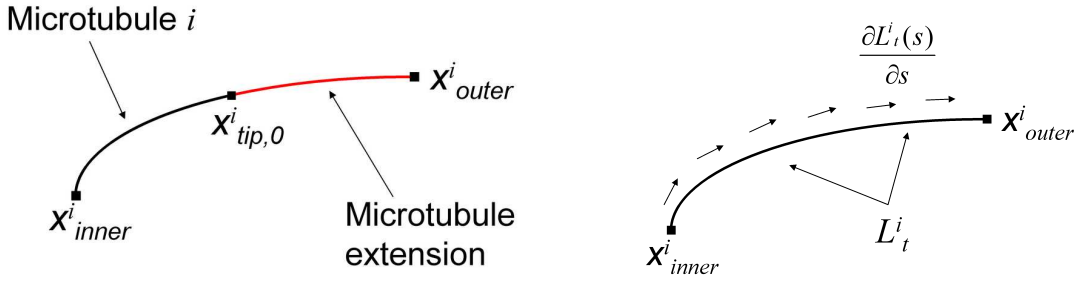

(a) Microtubule segmentation and extrapolation

(b) Curve expected to contain a microtubule tip

Fig. 5. In (a) is the segmentation of a microtubule at the first frame starting from $\mathbf{x}_{tip,0}^i$ until $\mathbf{x}_{inner}^i$. The microtubule is also extrapolated to get $\mathbf{x}_{outer}^i$. In (b) is the curve L_t^i along which a microtubule tip can lie at time t. Curve L_t^i is between boundary points $\mathbf{x}_{inner}^i$ and $\mathbf{x}_{outer}^i$.

The region where the i^{th} microtubule is expected to polymerize is estimated by extrapolating it starting from the microtubule outer tip point at the first frame, $\mathbf{x}_{tip,0}^i$. To extrapolate the microtubule we use a multiresolution approach in the temporal dimension by segmenting it over the average frame of the sequence $\mathcal{I}_{avg} = \sum_{t=0}^{\tau-1} \mathcal{I}_t$.

The segmentation algorithm used is that described in section 2.3 and gives $\mathcal{M}_p^i$. The point farther from $\mathbf{x}_{tip,0}^i$ along $\mathcal{M}_p^i$ is the farthermost point of the extrapolated microtubule and provides the outermost reference point $\mathbf{x}_{outer}^i$ for the computation of the trajectory of a microtubule outer tip. This is shown in figure 5 (a). An example of an image with extrapolated microtubules is shown in figure 2 (c). *To model the limited lateral motion that a microtubule can have we consider the region within $\nu = 2w$ around the extrapolated microtubule $\mathcal{M}_p^i$ to obtain the image domain in which the microtubule can polymerize, D_p^i.*

The length of the axes of both D_d^i and D_p^i is chosen to be $l = 8w$, which can adequately capture the cyclical motion of a microtubule in steady state for several minutes. The union of regions D_d^i and D_p^i gives the domain expected to contain the trajectory of the microtubule outer tip, $D_{traj}^i = D_d^i \cup D_p^i$. In that region the point $\mathbf{x}_{inner}^i$ is taken as a starting point to compute a cumulative cost map $U_{0,t}^i$, $\forall t$. *The cost along the microtubule axis is lower than it is in the background. This difference is robust both with respect to background noise and microtubule curvature.* Subsequently, we use this map to compute the minimal path L_t^i between $\mathbf{x}_{outer}^i$ and $\mathbf{x}_{inner}^i$. Both the cumulative cost and the curve are computed as described for microtubule segmentation in section 2.3. The curve L_t^i, $\forall t$, is expected to contain a microtubule as well as its tip. *The estimated region D_{traj}^i where a microtubule and its tip may lie obtained from low temporal resolution is restricted to a curve L_t^i in each frame*. An illustration showing curve L_t^i bounded by $\mathbf{x}_{inner}^i$ and $\mathbf{x}_{outer}^i$ is shown in figure 5 (b). An example of a frame from real data containing several curves L_t^i is shown in figure 2 (d).

2.6. Extraction of the Trajectories of Microtubule Tips

The intensities and differential characteristics along $L_t^i(s)$ at a tip point change from those of a microtubule to those of the cytoplasm or extracellular matrix. The sudden change is due to the large curvature of the isointensity contours at that point which causes a large increase in the value of the cost $U_{0,t}^i$. This change is used to compute a microtubule outer tip feature along $L_t^i(s)$, where s is the arc-length parameter. The tip feature $g_t^i(s)$ is the directional derivative of $U_{0,t}^i$ along the curve $L_t^i(s)$. That is:

$$g_t^i(s) = \nabla_{\frac{\partial L_t^i(s)}{\partial s}} U_{0,t}^i. \tag{6}$$

This feature is computed for frames $t = 1, \ldots, \tau - 1$. *It enhances the intensity of the tip point even though its signal to noise ratio is low. The feature is very robust not only to background noise, but also to microtubule curvature similarly to $U_{0,t}^i$ that was differentiated to compute it.*

The microtubule outer tip point in the first frame $t = 0$ is the starting point of the trajectory of the outer tip. The outer tip points $\mathbf{x}_{tip,t}^i$, $t = 1, \ldots, \tau - 1$ in subsequent frames are constrained to lie along L_t^i. The microtubule outer tip can only polymerize or depolymerize for a limited length ρ in the time interval between two consecutive frames. Thus, the tip position in a frame lies within a circle of radius ρ centered at the tip point in the previous frame $\mathbf{x}_{tip,t-1}^i$, $\left|\mathbf{x}_{tip,t}^i - \mathbf{x}_{tip,t-1}^i\right| \leq \rho$. The segment of the curve $L_t^i(s)$ enclosed by that circle gives the candidate tip positions at time t. The point in that curve segment that maximizes $g_t^i(s)$ is selected to give $\mathbf{x}_{tip,t}^i = \arg\max_{\mathbf{x} \in L_t^i(s)} g_t^i(s)$. This subsection together with the previous one, subsection 2.5, correspond to steps 3-5 of the algorithm shown in figure 6. These three steps are repeated sequentially for the extraction of the trajectories of the tips of the microtubules, $i = 0, \ldots, n - 1$.

2.7. Statistics of the Trajectories of the Microtubule Outer Tips

As a result of tracking the outer ends of the microtubules we can directly compute the microtubule lengths between the inner reference point $\mathbf{x}_{inner}^i$ and the tip $\mathbf{x}_{tip,t}^i$ along the microtubule axis. We estimate the lengths of all the outer segments of the microtubules and in all frames from $l_t^i = \int_{\mathbf{x}_{inner}^i}^{\mathbf{x}_{tip,t}^i} \frac{dL_t(s)}{ds} ds$, $\forall i, t$. This method of measuring

the length of microtubules along their axes is a more accurate approximation than the currently used manual one which assumes that the length of the microtubule is the Euclidean distance between an inner reference point in the image and the manually annotated tip [9, 10, 11, 2, 3]. Thus, it ignores microtubule curvature.

The length measures are used to compute the average of the absolute value of the change of the length of the microtubules $\mu\left(\left|\frac{\Delta l}{\Delta t}\right|\right) = \frac{1}{m(\tau-1)}\sum_{i,t}|l_t^i - l_{t-1}^i|$. This represents the average polymerization and depolymerization rate of the microtubules. The time series l_t^i is transformed over the time parameter to compute its Fourier spectrum G_f^i, where f is the temporal frequency. This gives the power spectral density $\Psi_{l_t^i}(f) = \|G_f^i\|^2, \forall i$, of microtubule length variation. *The sinusoidal approximation to the motion of a microtubule tip represents its cyclical motion in steady state. It also represents possible acceleration in polymerization and depolymerization.* Each motion frequency is weighted by the corresponding density to compute the average weighted frequency $f_{wt}^i = \sum_f f\Psi_{l_t^i}(f)$, $\forall i$. The global weighted frequency average over all the microtubules, $\mu(f_{wt}) = \frac{1}{n}\sum_i f_{wt}^i$, is also computed. *This can give an average representative value for the tip dynamics in a region of the cytoplasm.*

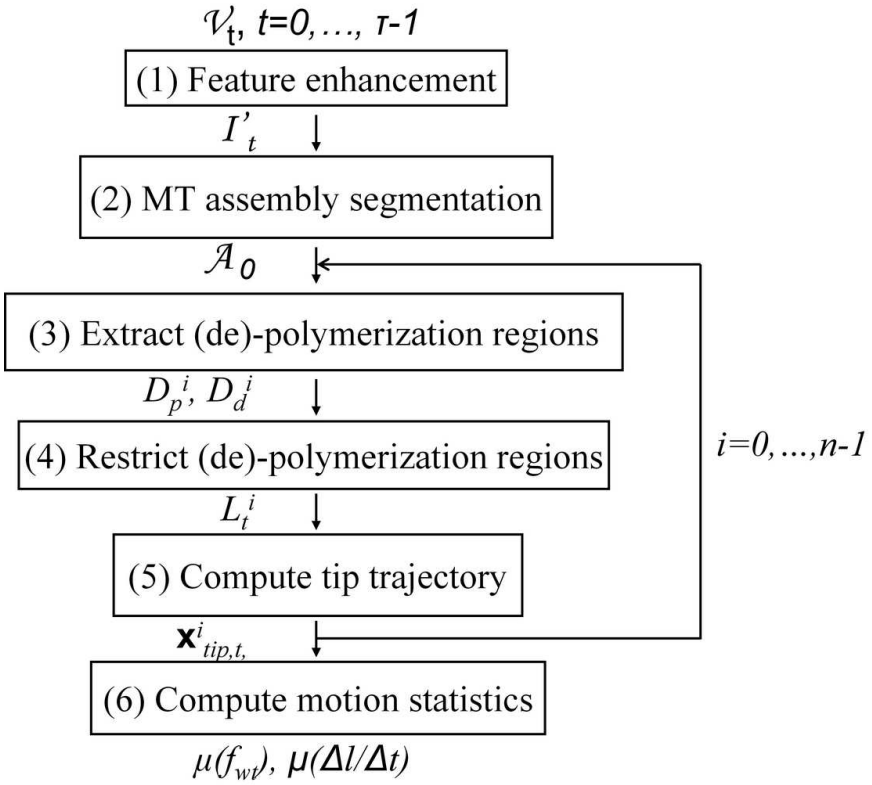

Fig. 6. This figure shows a block diagram summary of the algorithm. The microtubule enhancement and segmentation are performed at steps 1-2. Subsequently, steps 3-5 of the algorithm are repeated sequentially to extract the motion of the microtubule tips $i = 0, \ldots, n-1$. The last step is the extraction of the average motion statistics of the assembly.

3. EXPERIMENTS

The experiments were performed on a Xeon CPU of $2.40\ GHz$ and $1.00\ GB$ of RAM. The algorithm was implemented using the C++ programming language and *the user interface for the selection of the microtubule tips in the first frame was implemented in Tcl/Tk.*

3.1. Phantom Data

We tested the sensitivity of the system with two parameterized sets of phantom image sequences of microtubule dynamics. To model the imaging process the phantom image sequences were corrupted. They were first smoothed with a Gaussian filter of standard deviation 1.5. Subsequently, Gaussian noise was superimposed. The signal to noise ratio SNR is the ratio of the phantom microtubule intensity to the standard deviation of the Gaussian noise. All the phantom image sequences consist of 100 frames of spatial size 150×150. To evaluate the performance of the algorithm we measure the error in tip position per frame and per tip as a function of the phantom set parameter. The error is computed using the ground truth in the phantom data.

The first set of phantom sequences tested the sensitivity of microtubule tip tracking under superimposed Gaussian noise. A set of phantom image sequences with noise in the range $SNR = 5 - 50$ was used. Each sequence contained five microtubules. The microtubules were sinusoidal curves. Thus, the segments of the microtubules close to their tips deform as the microtubule polymerizes. The tenth and last frames of the phantom image sequence for $SNR = 6.25$ are shown in figure 7. In the first row, in figures 7 (a) and (b), are the images showing the tip positions computed by the algorithm in different colors. Figures 7 (c) shows the tip trajectories computed by the algorithm in red together with the ground truth trajectories of the tips in green. These images show the accuracy of the tracking for this sequence. The error of the tip positions as a function of the SNR is shown in figure 7 (d). *The algorithm accurately tracks the microtubule tips up to very low SNR, lower than the typical SNR of a confocal microscopy sequence*. The average computation time for each phantom sequence was $2\ min\ 46\ sec$.

The second set of phantom image sequences examined the sensitivity of the algorithm with respect to the proximity between neighboring microtubules. Each phantom sequence contained five microtubules. The microtubules were straight lines. The noise level was $SNR = 20$ and the microtubule width was $w \approx 5$. The distance between the axes of consecutive microtubules was in the range of $\delta = 4 - 10$ pixels. The fiftieth and last frames of the sequence with proximity $\delta = 7$ pixels between microtubules are shown in figure 8 (a) and figure 8 (b), respectively. The same images show the tip positions computed by the algorithm in different colors. In figure 8 (c) are the trajectories of the microtubule tips in red together with the ground truth in green. These images show that in this sequence for $\delta = 7$ the tracking is accurate. Figure 8 (d) shows a plot of the error in tip position as a function of the proximity between neighboring microtubules. *That plot demonstrates that the tracking algorithm succeeds for distance $\delta > w$ between neighboring microtubules. That is, when the distance between the axes of neighboring microtubules is greater than the standard deviation of their Gaussian cross sections. This shows the robustness of the tracking with respect to the proximity of neighboring microtubules.* The average computation time for each phantom sequence was $2\ min\ 38\ sec$. This is very low, which shows the limited computational requirements of the algorithm.

3.2. Real Microscopy Data

The algorithm was evaluated with several video sequences of real cells. Four of these sequences are shown in this work. In figure 10 and figure 11 we show two examples of our in-vivo imaging experiments of microtubule dynamics. The sample preparation and data acquisition were performed similarly to previously described at [57], expect that epithelial PtK2 cells that stably expressed α-tubulin-yellow fluorescent protein (YFP) were used. The cells were grown in Mattek coverslip dishes at 5% CO_2 in MEM containing 10% FCS, Pen-Strep, and $1\times$ non-essential acids. The cells were transferred for fluorescent imaging to an Olympus IX-70 microscope that had a custom plexiglass box and heater to maintain the cells at 37^oC in 5% CO_2. Typically, cells were excited by a shuttered monochromator (Till Photonics at wavelength $514\ nm$), Chroma YFP dichroic cube, and an $100\times$ 1.4 NA oil immersion objective lens. They were detected with an Orca-ER style CCD camera (PCO). The samples were illuminated for $50 - 100\ ms$ and the data was acquired every $5\ sec$ for several minutes.

The algorithm was verified with two additional imaging sequences. The imaging conditions of the sequence in figure 9 are described at [58]. It was an A6 line cell, that is, a Xenopus kidney epithelial cell. It expressed green

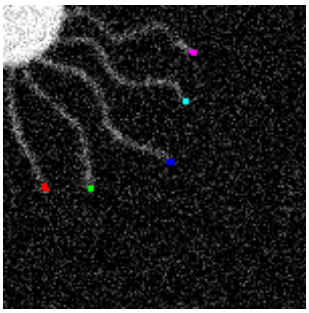

(a) Computed tips in tenth frame

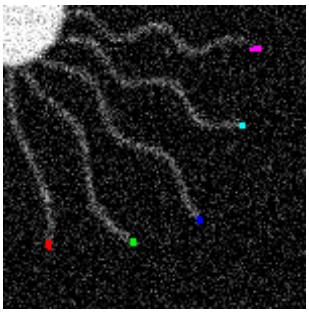

(b) Computed tips in last frame

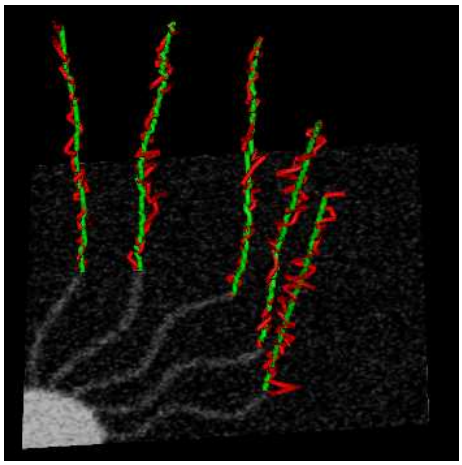

(c) Complete trajectories for the sequence

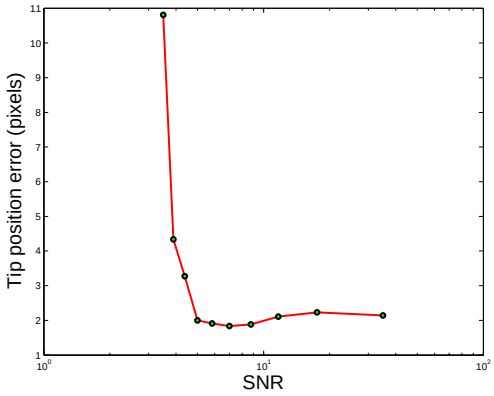

(d) Error with respect to SNR in logarithmic scale

Fig. 7. The images in the first row show the tenth and last frames of the phantom sequence for $SNR = 6.25$. The same images show the computed positions of the tips in different colors. The image in (c) is a spatiotemporal viewpoint of the computed tip trajectories in red together with the ground truth in green. In (d) is the error of the tip positions per frame and per tip as a function of SNR.

fluorescent protein that was fused by means of a $4\times$ Gly spacer to the C-terminus of β-tubulin, β-tubulin-GFP. The cells were cultured at 23^oC without CO_2 atmosphere. Fluorescent live imaging at room temperature of the cells was performed using DeltaVision full spectrum optical sectioning microscope system of Applied Precision, Inc. The microscope was equipped with an Olympus IX70 PlanApo, and an $100\times$ 1.40 NA oil immersion objective lens. The cells were detected with a cooled CCD camera of Quantix-LC, Photometrics. Time lapse recording was performed at $10\ sec$ intervals. The same microscope system was used to convert the sequence of images into a QuickTime movie using JPEG compression. The sequence shows the dynamics of microtubule plus ends next to a wounded edge of the cell.

The imaging conditions of the sequence in figure 12 are described in detail at [14]. They were live Schneider Drosophila S2 cells that stably expressed enhanced green fluorescent protein (EGFP)-tagged α-tubulin. It was cultured in Schneiders Drosophila medium supplemented with 10% heat-inactivated FCS and penicillin/streptomycin. A member of the kinesin-13 family, KLP59C, had been depleted using double-stranded (ds)RNA interference (RNAi). Samples were mounted in Prolong (Molecular Probes) and imaged with a spinning disk confocal scanner (Ultraview/Perkin Elmer, Boston, MA) mounted on a Nikon TE200 inverted microscope PlanApo with an $100\times$ 1.4 NA objective lens. Two z-sections of thickness $0.5\mu m$ were obtained with a piezo-electric z-axis controller for 4D data collection (x, y, z, time). Time lapse images were acquired at $1sec$ intervals. The images are presented as

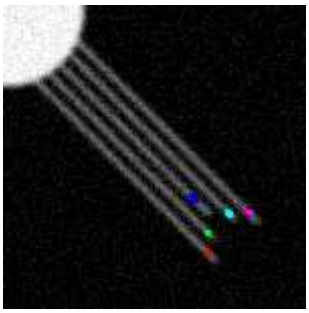

(a) Computed tips in fiftieth frame

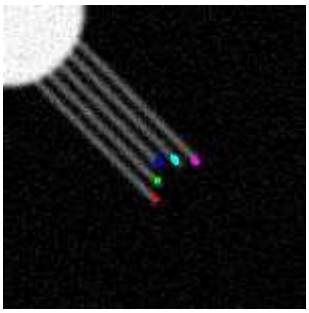

(b) Computed tips in last frame

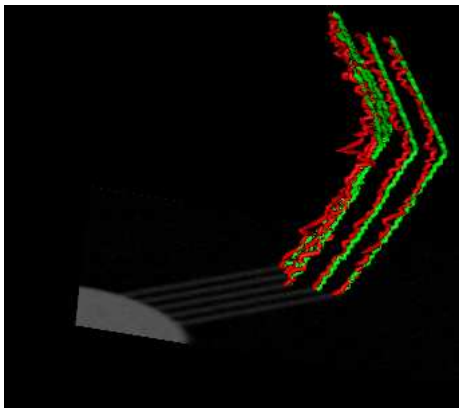

(c) Complete trajectories for the sequence

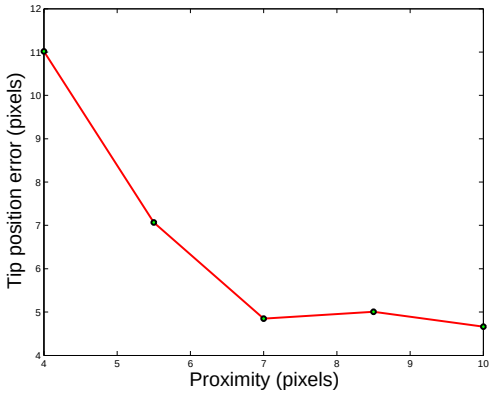

(d) Error with respect to proximity

Fig. 8. In the first row are the fiftieth and last frames of the phantom sequence for proximity $\delta = 7$ together with the computed positions of the tips in different colors. The image in (c) shows a spatiotemporal viewpoint of the computed tip trajectories in red together with the ground truth in green. In (d) is the error of the tip position per frame and per tip as a function of proximity.

the maximum intensity projections along the z axis. The sequence shows the dynamics of microtubule plus ends near the periphery of an extended region that contacted neighboring cells.

The sizes of all the sequences are in table 1. Two frames of each of the four sequences are shown in the first rows of figure 9, figure 10, figure 11, and figure 12, respectively. These figures show the tip positions in different colors for the tenth and last frames as computed by the algorithm. The majority of the computed tip trajectories were also traced manually with a mouse. The manual data was used as ground truth for performance evaluation. The entire trajectories of the tip points in the sequences are shown in red in spatiotemporal space in figure 9 (c), figure 10 (c), figure 11 (c), and figure 12 (c), respectively. In the same figures are also the manually annotated ground truth trajectories in green. These figures show that the trajectories of the tips were tracked accurately.

The statistics of the computed tip dynamics are given in table 1. These included the average of the absolute value of the change of the length of the microtubules $\mu\left(\left|\frac{\Delta l}{\Delta t}\right|\right)$. *They also include the weighted average of the frequency* $\mu(f_{wt})$ *of the motion power spectral density of all the microtubules in a sequence.* The tips for which the tracking error compared to ground truth was less than ten pixels were considered as having been tracked correctly. Those tips were used to compute the tracking error per frame and per tip. The statistics of the evaluation of tracking are also in table 1. *The error in tracking is very low. The large majority of microtubules were tracked*

Sequence	figure 9	figure 10	figure 11	figure 12
Size x-y	350×262	636×472	640×512	137×113
Size t	36	100	100	100
Δt is seconds	10	5	5	1
Tips tracked	8	19	13	10
Tips tracked correctly	7/8	16/19	11/13	8/10
Evaluation error (pixels)	3.4	2.4	3.7	3.2
$\mu\left(\left\|\frac{\Delta l}{\Delta t}\right\|\right)$ ($\mu m.s^{-1}$)	0.051	0.21	0.20	0.10
$\mu(f_{wt})$ (s^{-1})	2.00	4.10	2.91	2.00
Run time	2 min 19 sec	18 min 7 sec	27 min 9 sec	2 min 54 sec

Table 1. The statistics describing the real sequences. The table also summarizes the output of the algorithm, the performance of the algorithm, as well as its evaluation for the same sequences.

correctly. The algorithm is robust to microtubule proximity, low signal to noise ratio, and curvature at the tip point.

The algorithm has mainly failed to track microtubules that overlap. The outer microtubule tips tend to meet other microtubules and polymerize along their axes. As a result multiple microtubules can follow the same track and become indistinguishable with the imaging technique used. For the same reason the manual tracing of microtubules [9, 10, 11, 2, 3] is done for clearly distinguished microtubule tips. It has not been investigated whether ignoring overlapping microtubules introduces a bias in the estimates of the microtubule dynamics. The algorithm has also limited ability to resolve the trajectories of tips which intersect under a low angle. Table 1 gives the computation time of the algorithm; it is very short and depends on the size of the data.

4. SUMMARY AND DISCUSSION

The microtubule assembly plays numerous critical roles in a cell. It provides structure and support to the cell. It also coordinates cell migration and cell division. The most dynamic part of the microtubules are their outer tips. The assembly is also involved in pathological cell states, for example in neurodegenerative diseases and cancer. The microtubule assembly must be studied in a quantitative, high throughput, and informative manner. To this end we have developed a system for the semi-automatic tracking of the motion of the microtubule outer tips in a frame sequence. *The first step of the system is to enhance the signal to noise ratio of the microtubule assembly in the sequence. Subsequently, the microtubules are segmented in the first frame to compute the regions expected to contain the microtubules' trajectories of possible depolymerization. The microtubules are also segmented in low temporal resolution using the average frame of the sequence to compute the regions expected to contain the tips' trajectories for possible polymerization. Those regions are further restricted to a curve in every frame and a microtubule tip feature is computed along those curves. The tip features are linked to form the microtubule outer tip trajectories. The tracking starts at the first frame and progresses sequentially between consecutive frames. The tips' trajectories are summarized to give average statistics of the dynamics of the tracked microtubules.*

The algorithm we suggest significantly improves quantification compared to manual tracing which is currently used to measure microtubule polymerization and depolymerization rates. Our system performs automatic tracking of multiple tips in the same sequence over extended time periods. It also improves accuracy in polymerization and depolymerization rate estimates by measuring microtubule length using their axis. In addition, the system improves objectivity in quantification by performing tip detection using the high curvature of the isointensity contours at the tip point. That point is defined using not only intensity, but also its geometric differential properties.

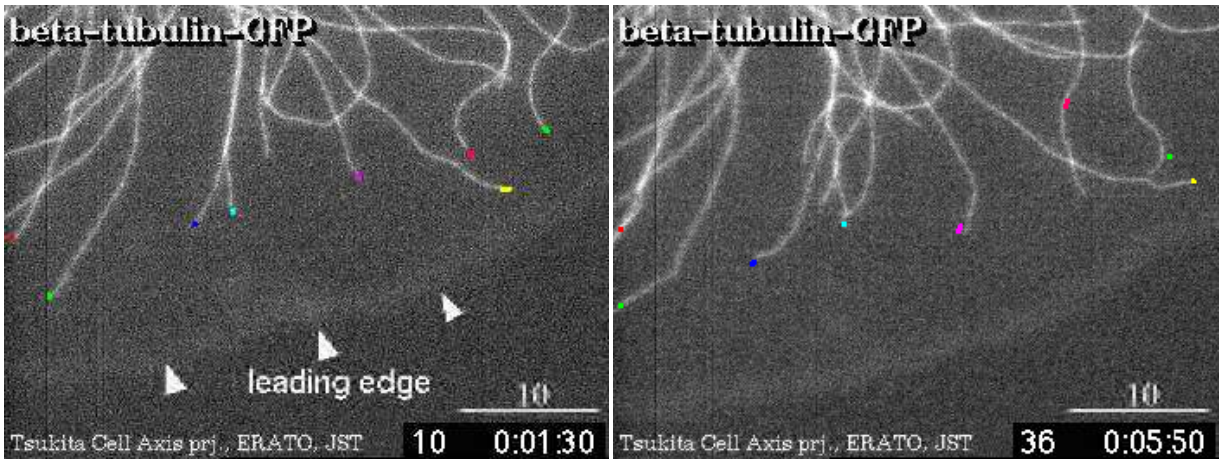

(a) Tips in tenth frame (b) Tips in last frame

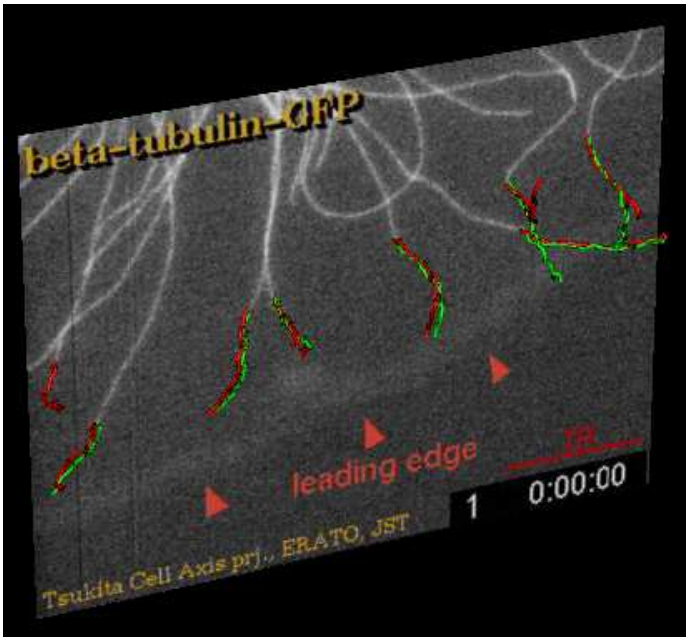

(a) A spatiotemporal viewpoint of the trajectories

Fig. 9. A Xenopus frog epithelial cell imaged with epifluorescent microscopy [58]. The images in the first row show the tenth and last frames together with the computed positions of the tips in different colors. In (c) is a spatiotemporal viewpoint of the tip trajectories. In red are the computed trajectories and in green are the manually tracked ones.

The system depends on four user set parameters. The parameter ranges capture the variability among microtubule tracking video sequences. The main parameter of the algorithm is the microtubule width, w*. The actual width of the microtubule is* $\approx 25\ nm$*. However, its width in an image depends on the spatial resolution and diffraction of the imaging process. The second parameter of the algorithm is the maximum allowed extent of polymerization or depolymerization of a tip. For the sequences tracked in this work it was set to* $8w$*. This parameter must be larger that the most extensive depolymerization or polymerization expected to be tracked. However, it must not be unnecessarily large to maintain the high signal to noise ratio required to compute the microtubule tip*

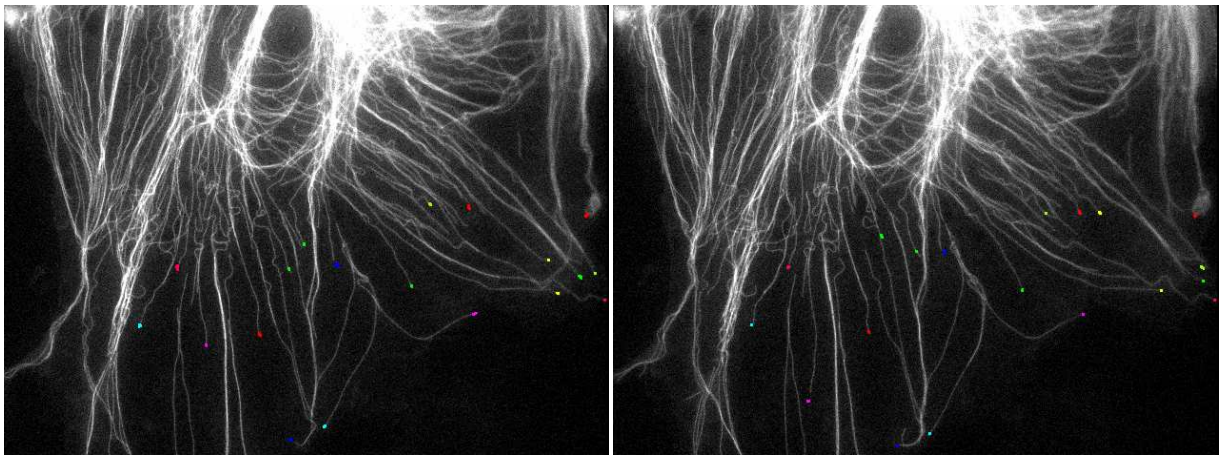

(a) Tips in tenth frame (b) Tips in last frame

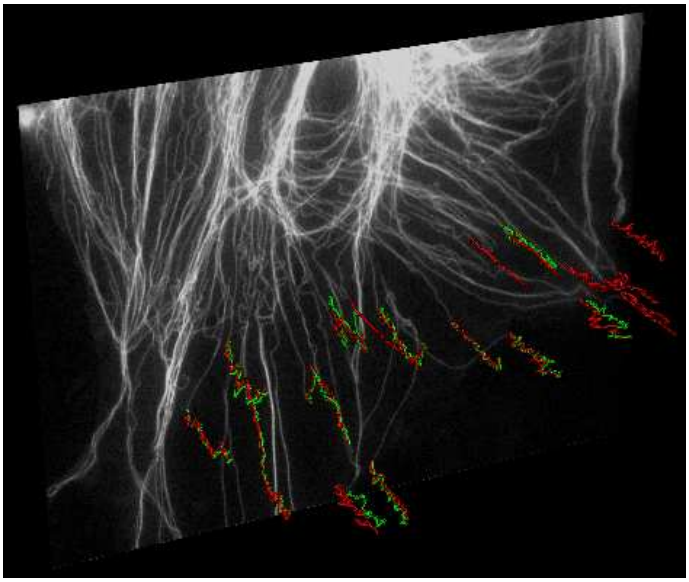

(a) A spatiotemporal viewpoint of the trajectories

Fig. 10. A rat epithelial cell imaged with epifluorescent microscopy. The images in the first row show the tenth and last frames together with the computed positions of the tips in different colors. In (c) is a spatiotemporal viewpoint of the tip trajectories. In red are the computed trajectories and in green are the manually tracked ones.

feature. The third parameter is the maximum allowed cumulative lateral displacement of a microtubule during the entire sequence. In this work it was set to $\nu = 2w$*. The values of the second and third parameters must increase with the total time duration of the acquisition of the sequence. The last parameter is the maximum allowed polymerization or depolymerization of a microtubule tip along its axis between two consecutive frames,* ρ*. It depends on the time interval between the acquisition of two consecutive frames.*

The algorithm was evaluated with phantom as well as real sequences. The large majority of the microtubules were tracked accurately. The algorithm is unable to resolve the trajectories of tips that overlap the axis of pre-existing microtubules. The tracking, however, was very robust with respect to image noise, proximity between neighboring microtubules, and curvature changes of the microtubules close to their outer tips. Moreover, the tip tracking was successful for high rates of polymerization and depolymerization and the algorithm was time effi-

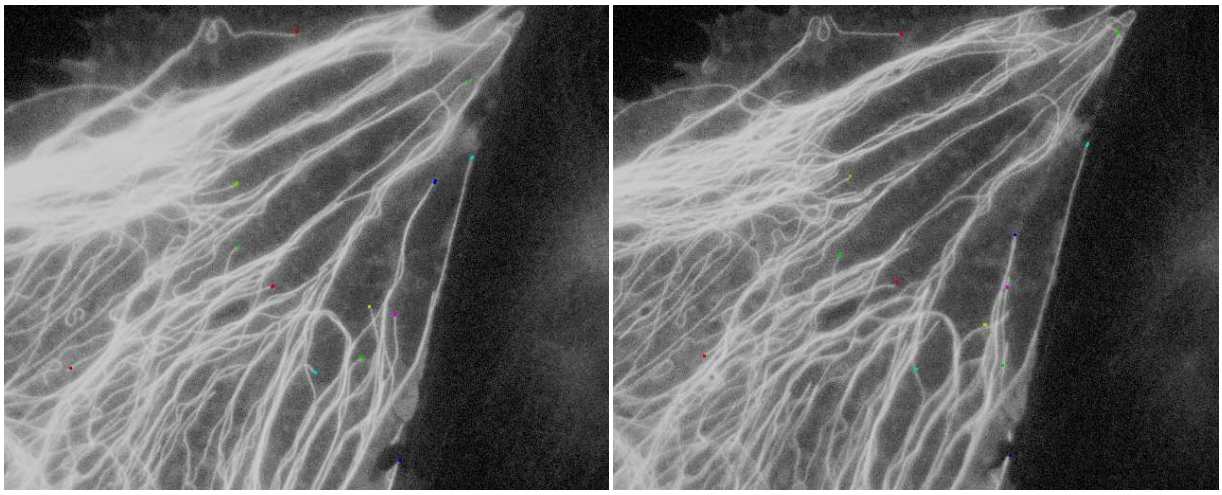

(a) Tips in tenth frame (b) Tips in last frame

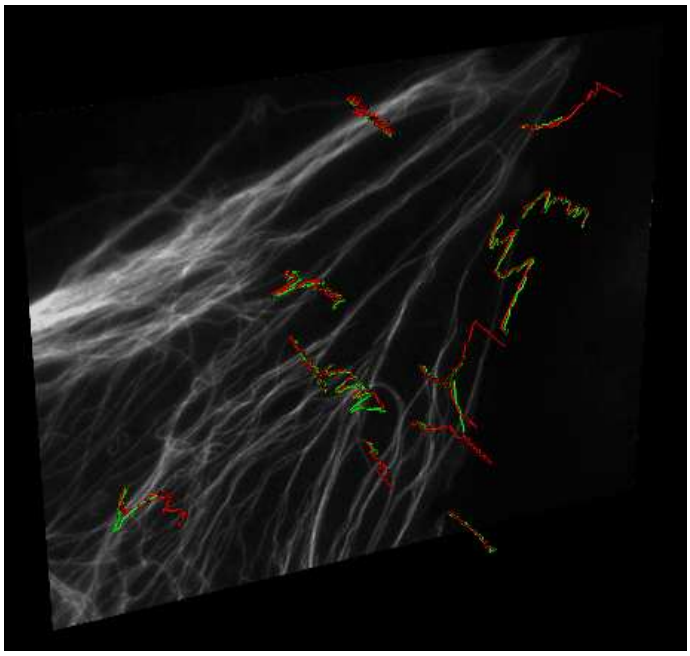

(a) A spatiotemporal viewpoint of the trajectories

Fig. 11. A rat epithelial cell imaged with epifluorescent microscopy. The images in the first row show the tenth and last frames together with the computed positions of the tips in different colors. The two images were histogram equalized to improve visualization. In (c) is a spatiotemporal viewpoint of the tip trajectories. In red are the computed trajectories and in green are the manually tracked ones.

cient. Also, the time duration of the tracking is adequate to allow microtubule studies of biological significance as well as studies for the development of new microtubule based drugs for cancer treatment. *The algorithm can be improved in several ways. One possibility would be to use different tracking modes for polymerization rather than for depolymerization [45]. This could represent the fact that the depolymerization speed is higher than the polymerization speed. Another possibility would be to perform quantum analysis to enable the resolution of overlapping microtubules. The motion tracking can be further improved by incorporating into the algorithm microtubule properties established in parallel in microtubule biology. That is, incorporate into the algorithm probabilistic priors*

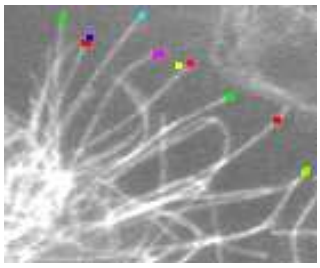

(a) Tips in tenth frame

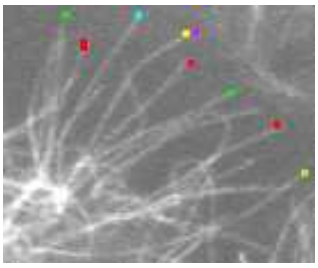

(b) Tips in last frame

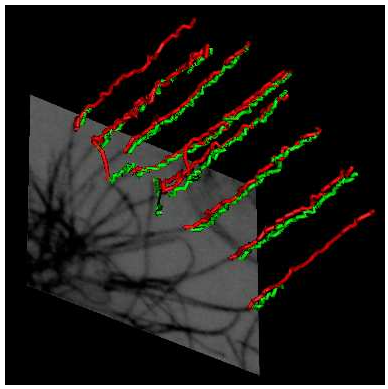

(a) A spatiotemporal viewpoint of the trajectories

Fig. 12. A melanogaster cell depleted of the kinesin-13 family member KLP59C imaged with spinning disk confocal microscopy [14]. The sequence consists of the maximum intensity projections of the data. The images in (a) and (b) show the tenth and last frames together with the computed positions of the tips in different colors. In (c) is a spatiotemporal viewpoint of the tip trajectories. In red are the computed trajectories and in green are the manually tracked ones.

about microtubule structure and motion.

5. REFERENCES

[1] A. Desai and T.J. Mitchison, "Microtubule polymerization dynamics," *Annual Review of Cell and Developmental Biology*, vol. 13, pp. 83–117, 1997.

[2] F. Verde, J.C. Labbe, M. Dore, and E. Karsenti, "Regulation of microtubule dynamics by cdc2 protein kinase in cell-free extracts of xenopus eggs," *Nature*, vol. 343, pp. 233–238, 1990.

[3] F. Verde, M. Dogterom, E. Stelzer, E. Karsenti, and S. Leibler, "Control of microtubule dynamics and length by cyclin a- and cyclin b-dependent kinases in xenopus egg extracts," *The Journal of Cell Biology*, vol. 118, no. 5, pp. 1097–1108, 1992.

[4] A. Kodama, T. Lechler, and E. Fuchs, "Coordinating cytoskeletal tracks to polarize cellular movements," *The Journal of Cell Biology*, vol. 167, no. 2, pp. 203–207, 2004.

[5] H. Braak and E. Braak, "Staging of Alzheimer's disease-related neurofibrillary changes," *Neurobiology of Aging*, vol. 16, pp. 271–278, 1995.

[6] D. A. Dabydeen, G. J. Florence, I. Paterson, and E. Hamel, "A quantitative evaluation of the effects of inhibitors of tubulin assembly on polymerization induced by discodermolide, epothilone b, and paclitaxel," *Cancer Chemotherapy and Pharmacology*, vol. 53, pp. 397–403, 2004.

[7] J. Howard and A.A. Hyman, "Dynamics and mechanics of the microtubule plus end," *Nature*, vol. 422, pp. 753–758, 2003.

[8] P. Carvalho, J.S. Tirnauer, and D. Pellman, "Surfing on microtubule ends," *Trends in Cell Biology*, vol. 13, no. 5, pp. 229–237, 2003.

[9] R.A. Walker, E.T. O'Brien, N.K. Pryer, M.F. Soboeiro, W.A. Voter, H.P. Erickson, and E.D. Salmon, "Dynamic instability of individual microtubules analyzed by video light microscopy: rate constants and transition frequencies," *Journal of Cell Biology*, vol. 107, pp. 1437–1448, 1988.

[10] C.M.Waterman-Storer and E.D. Salmon, "Actomyosin-based retrograde flow of microtubules in the lamella of migrating epithelial cells influences microtubule dynamic instability and turnover and is associated with microtubule breakage and treadmilling," *Journal of Cell Biology*, vol. 139, pp. 417–434, 1997.

[11] C.M. Waterman-Storer, W.C. Salmon, and E.D. Salmon, "Feedback interactions between cell–cell adherens junctions and cytoskeletal dynamics in newt lung epithelial cells," *Molecular Biology of the Cell*, vol. 11, no. 7, pp. 2471–2483, 2000.

[12] G. Danuser, P.T. Tran, and E.D. Salmon, "Tracking differential interference contrast diffraction line images with nanometre sensitivity," *Journal of Microscopy*, vol. 198, no. 1, pp. 34–53, 1999.

[13] S. Hadjidemetriou, J. Duncan, D. Toomre, and D. Tuck, "Automatic quantification of microtubule dynamics," in *Proc. of the IEEE International Symposium on Biomedical Imaging*, 2004, pp. 656–659.

[14] V. Mennella, G.C. Rogers, S.L. Rogers, D.W. Buster, R.D. Vale, and D.J. Sharp, "Functionally distinct kinesin-13 family members cooperate to regulate microtubule dynamics during interphase," *Nature Cell Biology*, vol. 7, no. 3, pp. 235–245, 2005.

[15] A. Altinok, M. El-Saban, A.J. Peck, L. Wilson, S.C. Feinstein, B.S. Manjunath, and K. Rose, "Activity analysis in microtubule videos by mixture of hidden Markov models," in *Proc. of Conference on Computer vision and Pattern Recognition*, 2006.

[16] M. El-Saban, *Automated Microtubule Tracking and Analysis, Ph.D. Thesis*, University of California Santa Barbara, Electrical and Computer Engineering, 2006.

[17] M. Saban, A. Altinok, A. Peck, C. Kenney, S. Feinstein, L. Wilson, K. Rose, and B.S. Manjunath, "Automated tracking and modeling of microtubule dynamics," in *Proc. of International Symbosium on Biomedical Imaging*, 2006.

[18] N. Lichtenstein, B. Geiger, and Z. Kam, "Quantitative analysis of cytoskeletal organization by digital fluorescent microscopy," *Cytometry Part A*, vol. 54A, pp. 8–18, 2003.

[19] S.R. Aylward and E. Bullitt, "Initialization, noise, singularities, and scale in height ridge traversal for tubular object centerline extraction," *IEEE Trans. on Medical Imaging*, vol. 21, no. 2, pp. 61–75, 2002.

[20] S.S. Work and D.M. Warshaw, "Computer-assisted tracking of actin filament motility," *Analytical Biochemistry*, vol. 202, pp. 275–285, 1992.

[21] J.S. Suri, K. Liu, and S. Laxminarayan, "A review on MR vascular image processing: Skeleton versus nonskeleton approaches: Part II," *IEEE Trans. on Information Technology in Biomedicine*, vol. 6, no. 4, pp. 338–350, 2002.

[22] F. Raisch, H. Scharr, N. Kirchgebner, B. Jahne, R.H.A. Fink, and D. Uttenweiler, "Velocity and feature estimation of actin filaments using active contours in noisy fluorescence image sequences," in *Proc. of Conference on Visualization, Imaging, and Image Processing*, 2002.

[23] H.J. Noordmans and A.W.M. Smeulders, "High accuracy tracking of 2D/3D curved line-structures by consecutive cross-section matching," *Pattern Recognition Letters*, vol. 19, pp. 97–111, 1998.

[24] M. Jiang, J. Qiang, and B.F. McEwen, "Enhancement of microtubules in EM tomography," in *Proc. of the International Symposium on Biomedical Imaging*, 2004, pp. 1123–1126.

[25] B. Stieltjes, W.E. Kaufmann, P.C. Zijl, K. Fredericksen, G.D. Pearlson, M. Solaiyappan, and S. Mori, "Diffusion tensor imaging and axonal tracking in the human brainstem," *Neuroimage*, vol. 14, pp. 723–735, 2001.

[26] L.D. Cohen and R. Kimmel, "Global minimum for active contour models: A minimal path approach," *International Journal of Computer Vision*, vol. 24, no. 1, pp. 57–78, 1997.

[27] T. Deschamps and L. Cohen, "Fast extraction of minimal paths in 3D images and applications to virtual endoscopy," *Medical Image Analysis*, vol. 5, pp. 281–299, 2001.

[28] T. Deschamps, R. Malladi, and I. Ravve, "Fast evolution of image manifolds and application to filtering and segmentation in 3D medical images," *IEEE Trans. on Visualization and Computer Graphics*, vol. 10, no. 5, pp. 525–535, 2004.

[29] C.J.M. Parker, C.A.M. Wheeler-Kingshott, and G.J. Barker, "Estimating distributed anatomical connectivity using fast marching methods and diffusion tensor imaging," *IEEE Trans. on Medical Imaging*, vol. 21, no. 5, pp. 505–512, 2002.

[30] J.M. Geusebroek, A.W.M. Smeulders, and H. Geerts, "A minimum cost approach for segmenting networks of lines," *International Journal of Computer Vision*, vol. 43, no. 2, pp. 99–111, 2001.

[31] O. Wink, W.J. Niessen, and M.A. Viergever, "Fast delineation and visualization of vessels in 3D angiographic images," *IEEE Trans. on Medical Imaging*, vol. 19, pp. 337–346, 2000.

[32] M. Jackowski, C.Y. Kao, M. Qiu, T. Constable, and L. Staib, "Estimation of anatomical connectivity by anisotropic front propagation and diffusion tensor imaging," in *Proc. of International Conference on Medical Image Computing and Computer Assisted Intervention*, 2004, pp. 663–671.

[33] L.M. Lorigo, O. Faugeras, W.E.L. Grimson, R. Keriven, R. Kikinis, and C.F. Westin, "Co–dimension 2 geodesic active contours for MRA segmentation," in *Proc. of the International Conference on Information Processing in Medical Imaging*, 1999, vol. 1613, pp. 126–139.

[34] E. Meijering, M. Jacob, J.-C.F. Sarria, P. Steiner, H. Hirling, and M. Unser, "Design and validation of a tool for neurite tracing and analysis in fluorescence microscopy images," *Cytometry Part A*, 2004.

[35] Y. Fridman, S.M. Pizer, S. Aylward, and E. Bullitt, "Segmenting 3D branching tubular structures using cores," in *Proc. of International Conference on Medical Image Computing and Computer Assisted Intervention*, 2003, vol. 2, pp. 570–577.

[36] G. Shechter, F. Devernay, E. Coste-Maniere, A. Quyyumi, and E.R. McVeigh, "Three-dimensional motion tracking of coronary arteries in biplane cineangiograms," *IEEE Trans. on Medical Imaging*, vol. 22, no. 4, pp. 493–503, 2003.

[37] N. Ritter, R. Owens, J. Cooper, R.H. Eikelboom, and P.P.V. Saarloos, "Registration of stereo and temporal images of the retina," *IEEE Trans. on Medical Imaging*, vol. 18, no. 5, pp. 404–418, 1999.

[38] F. Weichert, M. Wawro, and C. Wilke, "A 3D cardiovascular model for brachytherapy planning based on biplane angiography and intravascular ultrasound," in *Proc. of the International Conference on Computer Assisted Radiology and Surgery*, 2003, pp. 1398–2003.

[39] I. Weber and R. Albrecht, "Image processing for combined bright-field and reflection interference contrast video microscopy," *Computer Methods and Programs in Biomedicine*, vol. 53, pp. 113–118, 1997.

[40] S. Bonneau, M. Dahan, and L.D. Cohen, "Single quantum dot tracking based on perceptual grouping using minimal paths in a spatiotemporal volume," *IEEE Transactions on Image Processing*, vol. 14, no. 9, pp. 1384–1395, 2005.

[41] B.J. Schnapp, J. Gelles, and M.P. Sheetz, "Nanometer-scale measurements using video light microscopy," *Cell Motility and the Cytoskeleton*, vol. 10, pp. 47–53, 1988.

[42] R.N. Ghosh and W.W. Webb, "Automated detection and tracking of individual and clustered cell surface low density lipoprotein receptor molecules," *Biophysical Journal*, vol. 66, pp. 1301–1318, 1994.

[43] T. Schmidt, G.J. Schutz, W. Baumgartner, H.J. Gruber, and H. Schindler, "Characterization of photophysics and motility of single molecules in a fluid lipid membrane," *Journal of Physical Chemistry*, vol. 99, pp. 17662–17668, 1995.

[44] S.N. Ngoc, F.B. Laugier, C. Boulin, and J.C. Olivo, "Adaptive detection for tracking moving biological objects in video microscopy sequences," in *Proc. of the International Conference on Image Processing*, 1997, vol. 3, pp. 484–487.

[45] A. Genovesio, T. Liedl, V. Emiliani, W.J. Parak, M. Coppey-Moisan, and J.C Olivo-Marin, "Multiple particle tracking in 3-D+t microscopy: Method and application to the tracking of endocytosed quantum dots," *IEEE Transactions on Image Processing*, vol. 15, no. 5, pp. 1062–1070, 2006.

[46] I.F. Sbalzarini and P. Koumoutsakos, "Feature point tracking and trajectory analysis for video imaging in cell biology," *Journal of Structural Biology*, vol. 151, pp. 182–195, 2005.

[47] A. Ponti, P. Vallotton, W.C. Salmon, C.M.Waterman-Storer, and G. Danuser, "Computational analysis of f-actin turnover in cortical actin meshworks using fluorescent speckle microscopy," *Biophysical Journal*, vol. 84, pp. 3336–3352, 2003.

[48] B.P. Helmke, A.B. Rosen, and P.F. Daviesyz, "Mapping mechanical strain of an endogenous cytoskeletal network in living endothelial cells," *Biophysical Journal*, vol. 84, pp. 2691–2699, 2003.

[49] S. Shemlon and S. Hawkins, "Non-rigid image alignment for layered cell representation and motion tracking," in *Proc. of the IEEE NE Bioengineering Conference*, 1996, pp. 125–126.

[50] M.J. Saxton and K. Jacobson, "Single particle tracking: Applications to membrane dynamics," *Annual Review of Biophysics and Biomolecular Structure*, vol. 26, pp. 373–399, 1997.

[51] H. Qian, M. Sheetz, and E.L. Elson, "Single particle tracking: Analysis of diffusion and flow in two-dimensional systems," *Journal of Biophysics*, vol. 60, pp. 910–921, 1991.

[52] S. Hadjidemetriou, D. Toomre, and J.S. Duncan, "Tracking the motion of the outer tips of microtubules," in *Proc. of the IEEE International Symposium on Biomedical Imaging*, 2006, pp. 530–533.

[53] C. Steger, "An unbiased detector of curvilinear structures," *IEEE Trans. of Pattern Analysis and Machine Intelligence*, vol. 20, pp. 113–125, 1998.

[54] S. Hadjidemetriou, J. Duncan, and D. Toomre, "Segmentation and 3D reconstruction of microtubules in total internal reflection fluorescence microscopy (TIRFM)," in *Proc. of the 8th International Conference on Medical Image Computing and Computer Assisted Intervention*, 2005.

[55] J.A. Sethian and A. Vladimirsky, "Ordered upwind methods for static Hamilton-Jacobi equations: Theory and algorithms," *SIAM Journal on Numerical Analysis*, vol. 41, no. 1, pp. 325–363, 2003.

[56] Q. Lin, *Enhancement, Extraction, and Visualization of 3D Volume Data*, Linkoping Studies in Science and Technology Dissertations. No. 824, 2003.

[57] D. Toomre, P. Keller, J. White, J. Olivo, and K. Simons, "Dual-color visualization of trans-golgi network to plasma membrane traffic along microtubules in living cells," *Journal of Cell Science*, vol. 112, no. 1, pp. 21–33, 1999.

[58] Y.M. Kiyosue, "Tsukita cell axis project," http://www.tsukita.jst.go.jp/kiyosue/cytoskeleton.html.